Available online at www.sciencedirect.com
SCIENCE DIRECT®
PERGAMON
International Journal of Heat and Mass Transfer 46 (2003) 4215–4228
International Journal of HEAT and MASS TRANSFER
www.elsevier.com/locate/ijhmt

# Entrainment in high-velocity, high-temperature plasma jets. Part II: computational results and comparison to experiment

R.L. Williamson *, J.R. Fincke, D.M. Crawford, S.C. Snyder, W.D. Swank, D.C. Haggard

*Idaho National Engineering and Environment Laboratory, P.O. Box 1625, Idaho Falls, ID 83415-2211, USA*

Received 5 June 2002; received in revised form 22 April 2003

**Abstract**

The development of a turbulent high-velocity, high-temperature argon plasma jet issuing into air has been computationally modeled using the computer program LAVA. LAVA is a comprehensive computational software program developed for flowing thermal plasmas in the absence of electromagnetic fields, with particular emphasis on plasma jets. The plasma is represented as a multicomponent chemically reacting ideal gas with temperature-dependent thermodynamic and transport properties. The plasma flow is governed by the complete transient, compressible Navier–Stokes equations in two-dimensions in the current simulation. Turbulence is represented by the $k$–$\varepsilon$ model. Neutrals, ions and electrons are considered as separate components of species of the mixture. General kinetic and equilibrium chemistry algorithms compute ionization, dissociation, recombination and other chemical reactions. Computational results and extensive comparisons with experimental data are presented. In particular the influence of inflow boundary conditions and the ability of the $k$–$\varepsilon$ turbulence model to describe entrainment with chemistry are examined.


*Keywords:* Thermal plasma; Plasma spray; Modeling; Jets; Entrainment

## 1. Introduction

The quality and subsequent performance of a thermal spray coating is directly determined by the distributions of velocity, temperature, size, and melt fraction of injected particulates when they impact the substrate. These distributions are the direct result of interactions with the high-velocity, high-temperature plasma jet. The models governing particle motion and heating have been well developed and include many of the special characteristics governing the interactions between a particle and a thermal plasma. These effects include very large temperature gradients, non-continuum effects, strongly varying plasma properties, thermophorsis, turbulent dispersion, etc. A theoretical description of these effects has been developed and discussed extensively by Pfender and Lee [1]. Their work on non-continuum effects [2,3] and the influences of varying plasma properties [4] on particle drag and heat transfer are widely used. Building on this work, realistic models of mass transfer and heterogeneous chemical reaction have also been incorporated [5–7]. Recently, the diffusion of reactants introduced at the particle surface, and the tracking of melting, vaporization, and resolidification interfaces coupled with the calculation of the temperature distribution within the particle, have been included [5,6].

The ability of these plasma–particle interaction models, that are now reasonably complete and sophisticated, to produce realistic computational results requires that the plasma flow field be accurately simulated. Because the process is most often performed in a laboratory environment with the plasma jet issuing into the surrounding air, this simulation must include the turbulent mixing of two dissimilar gas streams. Along with

* Corresponding author.
*E-mail address:* rlw@inel.gov (R.L. Williamson).

0017-9310/$ - see front matter © 2003 Elsevier Ltd. All rights reserved.
doi:10.1016/S0017-9310(03)00271-0

**Nomenclature**

| | |
|---|---|
| $A_{eq}$ | constant |
| $A_f$ | constant |
| $B_{eq}$ | constant |
| $C_{eq}$ | constant |
| $C_\mu$ | constant |
| $D$ | binary diffusivity ($m^2/s$) |
| $D_{eq}$ | constant |
| $E_{eq}$ | constant |
| $F_{eq}$ | constant |
| $k$ | turbulent kinetic energy ($m^2/s^2$) |
| $k_f$ | forward rate coefficient ($cm^3/gm\,mol\,s$) |
| $K_{eq}$ | equilibrium constant |
| $L$ | turbulence length scale (m) |
| MW | molecular weight (kg/kg mol) |
| $n_T$ | fitting parameter |
| $n_v$ | fitting parameter |
| $P$ | pressure (Pa) |
| $r$ | radial coordinate (m) |
| $R$ | radial location (m) |
| $S_n$ | swirl number |
| $T$ | temperature (K) |
| $v$ | axial velocity (m/s) |
| $y$ | axial coordinate (m) |
| $Z$ | constant |

*Greek symbols*

| | |
|---|---|
| $\delta_{0.1}$ | jet width at $v = 0.1v_0$ (m) |
| $\varepsilon$ | turbulence dissipation rate ($m^2/s^3$) |
| $\kappa$ | adjustable parameter |
| $\eta$ | constant |
| $\Theta$ | activation temperature (K) |

*Subscripts*

| | |
|---|---|
| f | forward |
| $i$ | species |
| in | torch inner face |
| 0 | centerline |
| out | torch outer face |
| w | wall |

the large density and velocity differences between the jet and its surroundings, this interaction is strongly influenced by dissociation and recombination chemistry. The corresponding energy pools associated with the arc gas ions and atomic oxygen and nitrogen formed by dissociation of entrained air represent a significant source and sink of energy. For example, consider the perfect mixing of equal masses of argon and air (approximately 40 mol% argon and 60 mol% air) at 10,000 and 300 K, respectively. At thermodynamic equilibrium the resulting mixture temperature is 4700 K. At this temperature essentially all of the oxygen is dissociated and about 12.5% of the nitrogen is dissociated. If the oxygen and nitrogen in the mixture did not dissociate the corresponding mixture temperature would be approximately 7000 K. A similar mixture starting with argon at 12,000 K results in a mixture temperature of 6250 K corresponding approximately to the measured [8] centerline condition at 3.8 cm for the jet studied here. If equilibrium prevails, the oxygen is completely dissociated, the nitrogen is 40% dissociated, and the argon that was initially 20% ionized is completely recombined. The energy release associated with recombination of the argon ions accounts for 60% of the energy that goes into dissociation while sensible heat accounts for the other 40%.

The model developed in this study considers only the plasma jet as it exists from the torch body, relying partly on experimental data taken near the torch exit to establish inflow boundary conditions. Thus the model is not fully predictive. A fully predictive simulation would necessarily include the arc–gas interaction region within the plasma torch body. Unfortunately a reliable calculation of the physics within the torch body is extremely complex involving unsteady arc discharge dynamics in three dimensions. There have been recent efforts to simulate the arc–gas interaction inside the torch e.g., [9–12], but they represent significant simplifications of real behavior. Such models are generally steady-state (ignoring arc dynamics), involve unknown and thus assumed boundary conditions (such as the current density profile at the cathode) and typically utilize a fictitious anode concept to approximate the arc attachment region. A lack of experimental data within the torch body makes it difficult to assess or justify such simplifications and assumptions. Since reliable experimental data for the peak temperature and the velocity profile very near the torch exit are available, there is less uncertainty in the plasma jet simulation, which is the focus of this investigation, when such data are used to guide the specification of inlet boundary conditions.

The turbulence model used in this study is a simple $k$–$\varepsilon$ type [13,14]. Limited comparisons with experimental data [14,15] have shown this model capable of reproducing the overall flowfield characteristics (temperature, velocity, entrainment) with fair accuracy, providing useful semi-quantitative results. Despite the fact that the validity of the $k$–$\varepsilon$ model is not universal, it represents a practical compromise between simplicity and much more complicated models. In fact, most attempts at modeling thermal plasma jets have employed a $k$–$\varepsilon$ formulation or a variation of $k$–$\varepsilon$ [16–19]. Other approaches, including a two fluid model [20], a three equation model [21], a four equation model [22], and an eight equation Reynolds' stress transport model have

also been tested [19]. No consensus has yet emerged as to the preferred approach. Turbulence modeling remains a controversial subject and simple one- and two-equation models of the $k$–$\varepsilon$ type are not fully satisfactory, nor are more complicated models, in general, even for simple incompressible flows. Since the turbulence model determines the diffusion rates of heat, momentum and species, it directly impacts the accuracy of the entire calculation. The application of existing turbulence models to thermal plasma flows must therefore be regarded as speculative. However, turbulent mixing is important and cannot be neglected hence $k$–$\varepsilon$ has been employed on a provisional basis in our thermal plasma jet simulation, at least until better models become available.

A goal of this study is to examine in some detail the ability and adequacy of $k$–$\varepsilon$ type turbulence models to describe plasma jet entrainment phenomena with chemistry. It is well known that $k$–$\varepsilon$ type approaches are better suited to cases in which the chemistry is slow compared with the fluid mechanics [23] and have serious deficiencies for flows with fast chemistry relative to mixing. In the slow chemistry limit extensive turbulent mixing and diffusional equilibration across the small turbulence scales occurs prior to chemical reaction. Unfortunately this is not the case occurring in the near field of the plasma jet, where the time scale for temperature equilibration exceeds the time scale for chemical reaction [8] by a factor of 10. In the jet far field, the slow chemistry limit may be approached. Hence $k$–$\varepsilon$ type models are expected to perform relatively poorly in the high-speed turbulent shear region of the thermal plasma jet. As we will show, an equally important issue in producing useful engineering results is the choice of inflow boundary conditions and their influence on computational results. In the following sections we will describe the model and compare a variety of computational results with experimental data.

## 2. LAVA background

LAVA is a fluid dynamics software program for simulating thermal plasmas containing entrained particles in the absence of electromagnetic fields. The computer program has been under continuous development at the Idaho National Engineering and Environmental Laboratory for approximately the last decade. LAVA is being developed primarily for plasma spray applications, with a particular emphasis on plasma jets. A fluid-particle approach is employed, similar to that used previously to model fuel sprays in internal combustion engines [24–26].

In LAVA, the plasma is represented as a continuous, multicomponent, chemically reacting ideal gas, governed by the complete, transient, compressible Navier–Stokes equations in two or three dimensions. Electrons, ions, and neutral atoms are treated as separate chemical species in the plasma mixture. Temperature-dependent thermodynamic and transport properties are included and will be described in detail below. Turbulence is approximated by either subgrid-scale or $k$–$\varepsilon$ models. Species diffusion is calculated by a self-consistent effective binary diffusion approximation [27], which has been shown to give reasonable accuracy for multicomponent diffusion thus providing a good compromise between accuracy and computing effort [28]. The diffusion model has also been generalized to allow for ambipolar diffusion of charged species. Ionization, dissociation, recombination, and other chemical relations are simulated using general kinetic and equilibrium chemistry algorithms. The plasma is presumed to be optically thin, thus radiative heat loss is modeled as a simple temperature-dependent volumetric sink term. The governing equations are solved using standard finite-difference techniques, with both transient and steady-state simulations possible. Detailed descriptions of the fluid dynamic and numerical solution aspects of LAVA have been given previously [13,14].

## 3. Model description

The geometry used in this study is consistent with a Miller SG-100 commercial torch discharging argon into ambient air. Specifically, an argon flow rate of 35.4 slm was used, while the torch was assumed to operate at 900 A and 15.4 V, with a thermal efficiency of 70%. The plasma flow was assumed to be steady, axisymmetric and described in two-dimensional cylindrical coordinates. As mentioned above, turbulence was approximated using a simple $k$–$\varepsilon$ model. The standard $k$–$\varepsilon$ model constants as given in [13,14] were employed. The effects of swirl were examined computationally using a realistic range of swirl numbers [14] ($S_n \leqslant 0.055$) and found to have little influence on this relatively low-velocity, low-swirl problem. Consequently swirl is not included in the computational results presented here. Gravity effects were also neglected. The plasma was assumed to be in thermal equilibrium (i.e., equal electron and heavy particle temperatures) since departures from thermal equilibrium in plasma jets in the absence of external electric or magnetic fields are generally negligible [29]. Chemical equilibrium is not assumed, and the chemistry reaction set is described below. Steady flow conditions were established after running a transient calculation for 3 ms.

### 3.1. Species and chemical reactions

In addition to the ionization–recombination of the argon arc gas, the important chemical reactions

Table 1
Chemical reactions and associated rate and equilibrium data

| Reaction | Rate coefficient ($k_f$)[a] | | | Equilibrium constant ($K_{eq}$) | | | | | |
|---|---|---|---|---|---|---|---|---|---|
| | $A_f$ | $Z$ | $\Theta$ (K) | $A_{eq}$ | $B_{eq}$ | $C_{eq}$ | $D_{eq}$ | $E_{eq}$ | $F_{eq}$ |
| $Ar + e^- \leftrightarrow Ar^+ + e^- + e^-$ | $5.7\times10^{8}$ | 1.5 | 135,300 | 1.5 | −183.0 | −6.49 | 0.0 | 0.0 | 0.0 |
| $N + e^- \leftrightarrow N^+ + e^- + e^-$ | $2.5\times10^{33}$ | −3.82 | 168,200 | 1.25 | −169.0 | −7.14 | 0.0 | 0.0 | 0.0 |
| $O + e^- \leftrightarrow O^+ + e^- + e^-$ | $3.9\times10^{33}$ | −3.78 | 158,000 | 1.75 | −158.0 | −9.60 | 0.0 | 0.0 | 0.0 |
| $N + N \leftrightarrow N_2^+ + e^-$ | $2.0\times10^{13}$ | 0.0 | 67,500 | 1.55 | −62.4 | −13.0 | 0.475 | −0.27 | 2.88 |
| $N_2 + M \leftrightarrow 2N + M$ | $7.0\times10^{21}$ | −1.6 | 113,200 | 0.795 | −113.0 | 3.17 | −0.444 | 0.027 | 0.0 |
| $O_2 + M \leftrightarrow 2O + M$ | $2.0\times10^{21}$ | −1.5 | 59,500 | 0.431 | −59.7 | 3.50 | −0.340 | 0.015 | 0.0 |
| $N_2 + N^+ \leftrightarrow N_2^+ + N$ | $9.9\times10^{12}$ | −0.18 | 12,100 | 1.10 | −6.96 | −2.66 | 0.031 | −2.88 | 0.0 |

[a] Units are $cm^3$, gm mol, K.

associated with the entrained air are also included. The species included in the present simulation are: Ar, $Ar^+$, $N_2$, $N_2^+$, N, $N^+$, $O_2$, O, $O^+$, and $e^-$. The interaction of these species is governed by means of separate kinetic chemical reactions, including ionization, dissociation, charge exchange, and dissociative recombination. The specific reaction set assumed appears in Table 1. Obviously, this set does not include all possible reactions in the plasma, but has been reduced for computational efficiency. With the exception of certain NO reactions, this reduced set corresponds to that recommended by Park et al. [30] who performed computational sensitivity studies to identify those reactions which exert a significant influence on main plasma parameters in a flowing jet. The formation of $NO_x$ is neglected in this study due to the small amount observed experimentally in thermal plasma jets [31] and the small amount of energy the reaction consumes. Atomic and molecular excited states and associated radiative processes are also neglected for simplicity.

The temperature-dependent forward rate coefficient for each of the N and O reactions is expressed in an Arrhenius form:

$$k_f(T) = A_f T^Z \exp\left(-\frac{\Theta}{T}\right) \tag{1}$$

where $A_f$ and $Z$ are constants, $T$ is the temperature, and $\Theta$ is the activation temperature. Constants were obtained from [30] and are included in Table 1. For the argon ionization reaction a form similar to that proposed by Hoffert and Lien [32] was employed:

$$k_f(T) = A_f T^Z \left(\frac{\Theta}{T} + 2\right) \exp\left(-\frac{\Theta}{T}\right) \tag{2}$$

Data for this equation, also shown in Table 1, where obtained from an experimental study by Owano and Kruger [33] and are very similar to those proposed earlier by Hoffert [34].

Equilibrium constants are represented by the following form:

$$K_{eq}(T) = \exp\left[A_{eq}\ln(T_A) + \frac{B_{eq}}{T_A} + C_{eq} + D_{eq}T_A + E_{eq}T_A^2 + \frac{F_{eq}}{T_A^2}\right] \tag{3}$$

where $T_A = T/1000$. Coefficients for the ionization reactions were obtained from the Saha equation [35], with the partition functions approximated by temperature-independent effective ground-level degeneracy factors [35]. For the molecular dissociation reactions, these data were obtained using the functional fits of Olikara and Borman [36] and, for the remaining reactions from Park [37]. Table 1 provides the constants used for all reactions. In the molecular oxygen and nitrogen dissociation reactions, the third body is represented by M, which includes all species. Third body efficiencies were obtained from [30]: for nitrogen dissociation, the efficiency for electrons is 1714.3, for N, $N^+$, O, and $O^+$ is 4.286, and for all other species is one; for oxygen dissociation, the efficiency for electrons is 45.2, for N, $N^+$, O, and $O^+$ is 5.0, and for all other species is one.

### 3.2. Geometry and computational mesh

The axisymmetric geometry and a representative computational mesh utilized in the simulations are shown in Fig. 1. The model considers only the plasma jet exiting the torch, thus the flow inlet plane of the model corresponds to the face of the torch body. The extent of the computational domain was 4 cm in the radial direction and 10 cm in the axial direction. The torch nozzle radius was 4 mm. Three different mesh densities ($49\times56$, $75\times86$, and $99\times110$, where the first value corresponds to the radial direction) were employed to establish numerical resolution of the model. For clarity, the coarser mesh ($49\times56$) is shown in Fig. 1. Each mesh was refined near the torch inlet and entrainment regions to better capture the large gradients in these areas.

Comparisons were made between the three mesh densities for a variety of results (temperatures, velocities, species densities, etc.). Differences between the $49\times56$

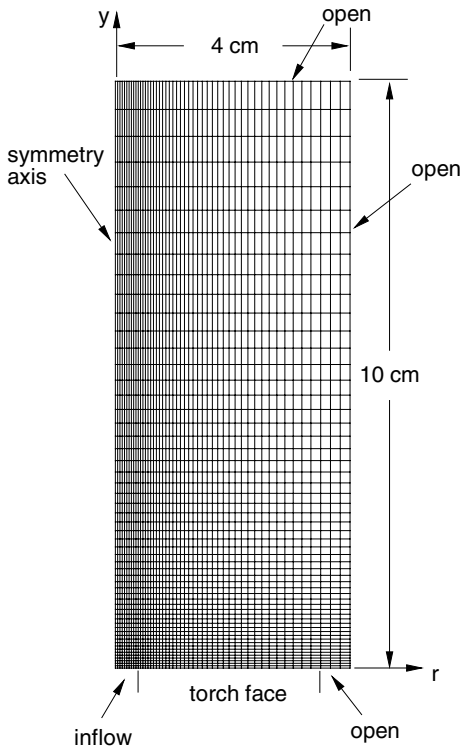


Fig. 1. The geometry, computational mesh, and boundary conditions utilized in the simulations.

and $75\times86$ meshes were significant, typically on the order of 15%, indicating inadequate resolution with the coarser mesh. Alternatively, differences were typically less than 5% between the two finer meshes, indicating either mesh is probably adequate. Based on these comparisons, all results presented in this study were obtained for the finest mesh ($99\times110$).

### 3.3. Thermodynamic and transport properties

The plasma thermodynamic pressure was related to temperature using an ideal gas law with temperature-dependent specific heats. For temperatures below 6000 K, species enthalpies were related to temperature using tabulated data [38]; above this temperature partition functions [39] were employed.

The effective binary diffusivities for the various species were calculated using the simple approximate formula [14]:

$$D_i = \eta\left(\frac{1}{\mathrm{MW}_i}+\frac{1}{\mathrm{MW}}\right)^{1/2}\frac{T^{3/2}}{P} \tag{4}$$

where $\mathrm{MW}_i$ is the molecular weight of species $i$, MW is the local mean molecular weight of the plasma exclusive of species $i$, $P$ is the pressure, and $\eta$ is a constant. In this study, $\eta$ was set to 0.002 $\mathrm{kg^{3/2}\,m\,s^{-3}\,K^{-3/2}\,kg\,mol^{-1/2}}$, which is a compromise value based on the binary and self diffusion coefficients for $N_2$, $O_2$, and Ar at 3500 K.

Based on the local argon mole fraction, the laminar viscosity and thermal conductivity of the mixture were obtained by interpolation between tabulated data for pure argon and air plasmas as functions of temperature [14]. This somewhat arbitrary approach is of course only approximate. The resulting mixture transport coefficients are probably reasonable, but are unlikely to be highly accurate. Since the calculations are turbulent, however, these laminar coefficients are small compared to the corresponding turbulent ones, so the calculation as a whole should be relatively insensitive to their precise values.

### 3.4. Initial and boundary conditions

The computational domain is initially filled with quiescent air at ambient temperature. Three different boundary condition types are employed in the model, namely torch face, open, and inflow. These are identified in Fig. 1, and described below.

The torch face was treated as a solid boundary. Wall temperatures were assumed to vary between 700 K at the nozzle boundary to 300 K at the torch face outer radius according to the following relation:

$$T = 700 - 400\frac{\ln(r/R_{\mathrm{in}})}{\ln(R_{\mathrm{in}}/R_{\mathrm{out}})} \tag{5}$$

where $r$ is the radial coordinate and $R_{\mathrm{in}}$ and $R_{\mathrm{out}}$ are the torch face inner and outer radii, respectively. This equation simply describes the steady-state radial temperature distribution for an annulus.

For the open boundaries, ambient pressure was assumed. Since the flow at these boundaries can be either outward or inward (entrainment), it was calculated rather than imposed. For outward flow, all other variables (including $k$ and $\varepsilon$) were assigned a zero-gradient condition. For inward flow, the inflowing gas was assumed to be ambient temperature air ($k=\varepsilon=0$) and enter the domain with a zero-gradient velocity in a direction normal to the boundary.

Because only the jet outside the torch nozzle was considered in the model, radial profiles of temperature, velocity, species densities and turbulence parameters ($k$ and $\varepsilon$) at the torch exit (or inlet to the flow model) are required as inflow boundary conditions. These profiles are constrained by the assumption of ionizational equilibrium and the known arc gas flow rates and torch power, but are otherwise unknown. The approach used for LAVA simulations is to assume forms for these profiles, subject to the above constraints and available experimental data. The temperature and axial velocity profiles at the torch exit plane ($y=0$) are assumed to have the forms:

$$T = (T_0 - T_w)[1 - (r/R_{in})^{n_T}] + T_w \quad (6)$$

$$v = v_0[1 - (r/R_{in})^{n_v}] \quad (7)$$

where $T_w$ is the torch wall temperature. The centerline values $T_0$ and $v_0$ and fitting parameters $n_T$ and $n_v$ were selected to match the known arc gas flow rates and torch power as closely as possible, by integrating the resulting mass and energy over the nozzle exit area. Experimental measurements [8] were used to guide this selection. Measurements along a radial profile 2 mm downstream from the torch face were well fit by inflow boundary profiles using $T_0$ and $n_T$ of 12,913 K and 2.3, respectively, and $v_0$ and $n_v$ of 1092 m/s and 1.4, respectively, Fig. 2. Note that these parameters are specific to the torch and operating conditions considered, and should not be expected to be accurate for other torches or other operating conditions. Because of the rapid mixing of the jet with the surrounding atmosphere, the calculation in the jet far field is not overly sensitive to centerline values of $v_0$ and $T_0$. The results are, however, somewhat more sensitive to the profile shape, which is determined by $n_v$ and $n_T$. With the inlet temperature profile established, inlet species density profiles were obtained by assuming ionization equilibrium and charge neutrality at ambient pressure. The radial velocity along the jet inflow boundary was assumed to be zero.

Information regarding inflow profiles of turbulence variables in plasma torches is generally not available. The inflow turbulent kinetic energy profile was simply assumed to have the form [15]:

$$k(r) = \kappa v_0^2 \left| \frac{\partial v}{\partial r} \Big/ \left( \frac{\partial v}{\partial r} \right)_{max} \right| \quad (8)$$

where $(\partial v/\partial r)_{max}$ is the largest axial velocity gradient with respect to the radial direction at the torch exit and $\kappa$ is an adjustable parameter. With $k(r)$ established, the inflow profile for $\varepsilon$, the turbulence dissipation rate, was then obtained using [40]: $\varepsilon = k^{3/2}/L$ with $L = 0.075\delta_{0.1}/c_\mu^{3/4}$ where $c_\mu = 0.09$ and $\delta_{0.1}$ is the jet width

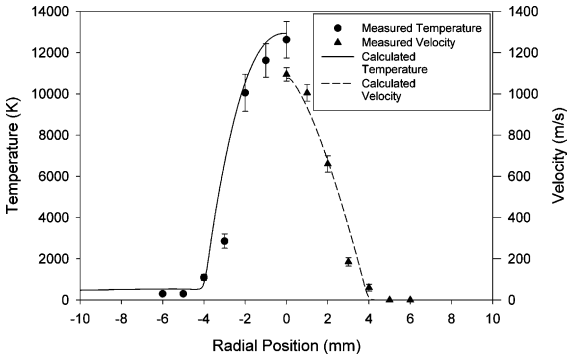


Fig. 2. Comparisons between measured and calculated velocity and temperature profiles at 2 mm downstream of the torch face.

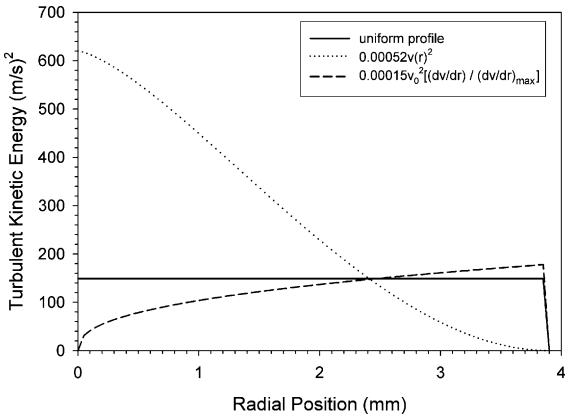


Fig. 3. Inflow turbulent kinetic energy profiles examined in this work.

defined by the location at which $v = 0.1v_0$. For the assumed velocity profile this form provides a turbulent kinetic energy profile that has a maximum value at the outer radius of the jet, but decreases to relatively small values near the jet axis, where the flow is expected to be nearly laminar [41,42]. This type of profile, Fig. 3, is consistent with experimental observation in both turbulent pipe flow and turbulent boundary layers [43] in that the maximum intensity of turbulence (and shear stress) is near the wall and falls off towards the centerline. In the central region viscous forces tend to reduce the turbulence intensity. In high temperature viscous plasma jets this is particularly true. The actual shape of the assumed profile only approximates experimental observation [43]. Since experimental data were not available to aid in the selection of $\kappa$, a variety of values ($\kappa = 0.0003$, 0.00015, 0.000075) were used to test sensitivity to this parameter. Some sensitivity was demonstrated and a value of $\kappa = 0.00015$ was selected because it was judged to give the best overall fit to the experimentally measured [8] velocity and temperature radial profiles at 2 mm (Fig. 2) and to the centerline decay of velocity, temperature, and entrained air fraction, Figs. 4–6. The fact that $k$ has an effect on simulation results, and experimental data is lacking to aid in its selection, is an important issue with regards to the predictive capability of the model.

The effect that other functional forms for $k(r)$ have on the results was also briefly examined. A uniform turbulence intensity profile and a form that is parabolic in $v(r)$ were tried, since recent simulations have been reported using these profiles [16,18,19]. In both cases, the magnitudes were chosen to give the same average turbulent kinetic energy ($k(r)$ integrated over the flow area) as the derivative based profile using $\kappa = 0.00015$. The three profiles considered are illustrated in Fig. 3 and centerline results are included in Figs. 4–6. As expected,

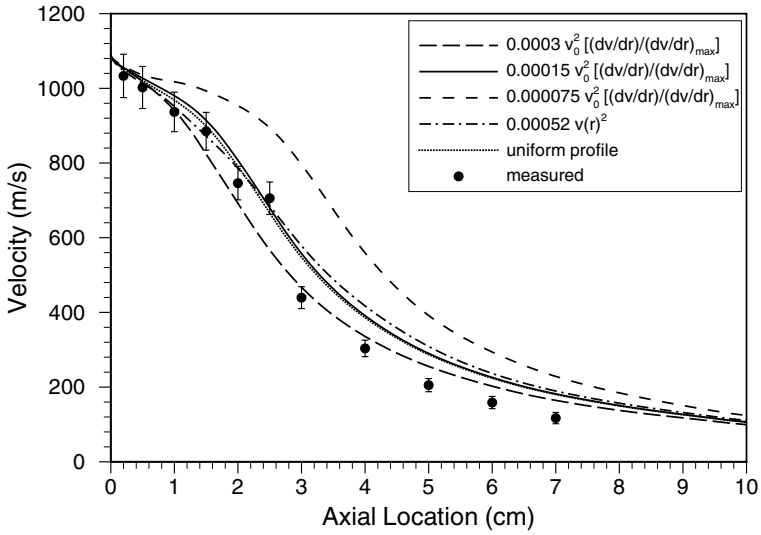


Fig. 4. Comparison between computational results and measured centerline velocity decay. The solid line result ($\kappa = 0.00015$) using the derivative based profile was chosen as the best overall fit to jet behavior.

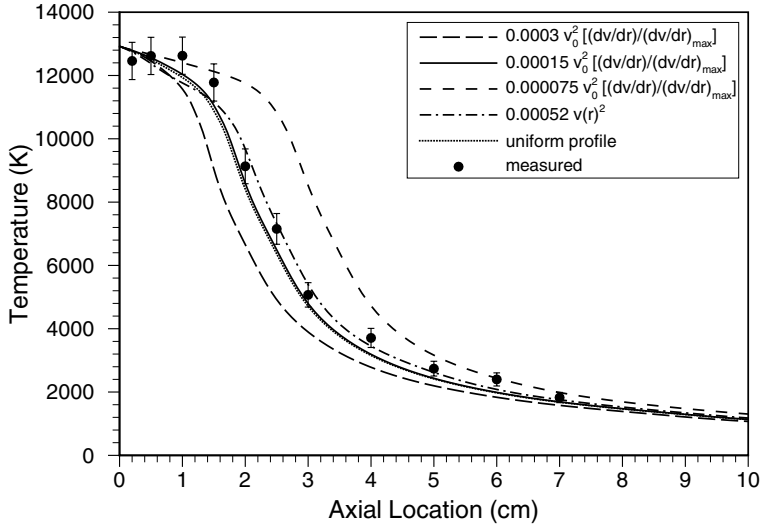


Fig. 5. Comparison between computational results and measured centerline temperature decay. The solid line result ($\kappa = 0.00015$) using the derivative based profile was chosen as the best overall fit to jet behavior.

the uniform profile produces behavior nearly identical to the derivative profile, primarily because it has very similar turbulent kinetic energy near the periphery of the jet. However, even the parabolic profile, having a shape completely different than the other profiles considered, did not result in large differences in centerline results. Note that a comparison to the experimental data, particularly for the velocity and air entrainment, tends to support the uniform or derivative profile over the parabolic form. However, one must be careful about reading too much into this comparison since other factors, such as dissociation rates and jet fluctuations, which were not parametrically studied, could also have a significant effect on the centerline results.

## 4. Comparisons to experiment

The comparisons to centerline decay of velocity, temperature and the entrainment of air have been

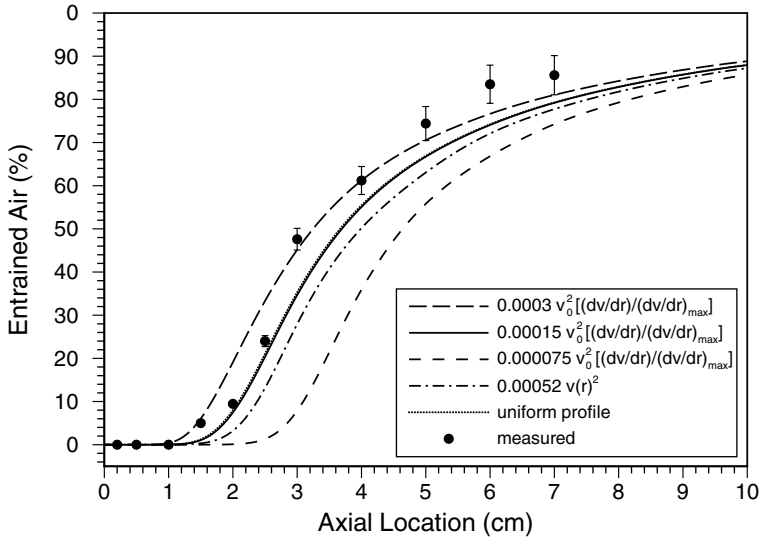


Fig. 6. Comparison between computational results and measured centerline entrainment of air. The solid line result ($\kappa = 0.00015$) using the derivative based profile was chosen as the best overall fit to jet behavior.

presented in Figs. 4–6 using the derivative based turbulent kinetic energy inlet profile with $\kappa = 0.00015$. This result is represented by the solid line in each figure, and was chosen as the best compromise fit to the experimental data.

Figs. 7 and 8 contain comparisons between centerline measurements [8] and calculated results for the oxygen chemistry. The molecular ($O_2$) and total ($O + 2O_2$) oxygen atom number densities are provided in Fig. 7. While the logarithmic ordinate, used because of the three order of magnitude range, makes the comparisons appear better than they actually are, the comparisons are still reasonable. For the atomic oxygen along the centerline, shown in Fig. 8, LAVA calculates a peak concentration that matches both the location and magnitude of the experimental data. The fact that the magnitude is reproduced so well is somewhat surprising, and is probably somewhat coincidental; it does suggest, however, that mixing and thermal equilibration of the small turbulence scales is reasonably complete on the centerline,

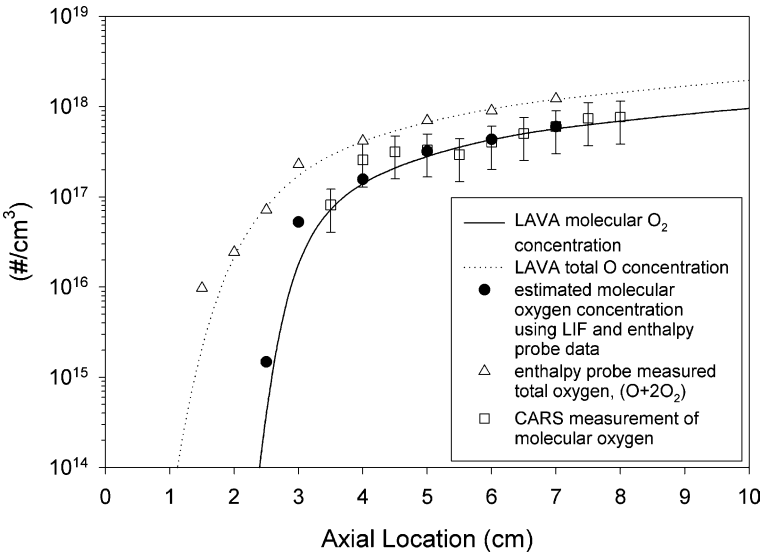


Fig. 7. Comparison between computational results and the measured centerline molecular and total oxygen concentrations.

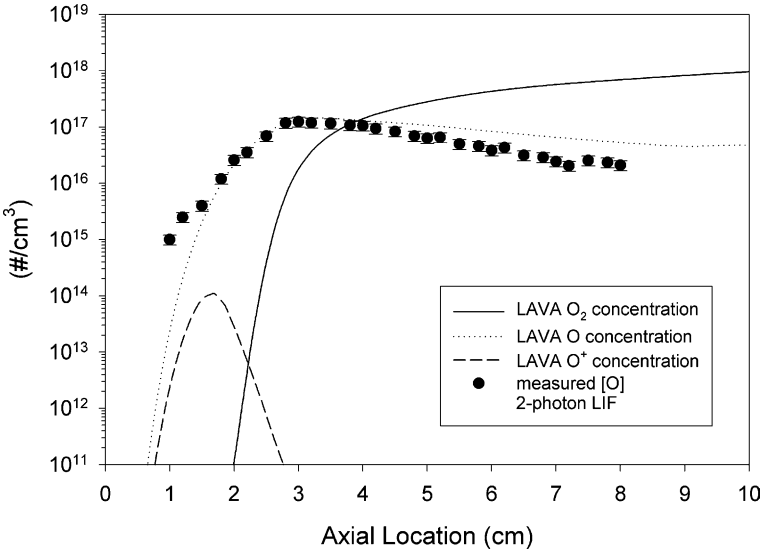


Fig. 8. Comparison between computational results and measured centerline atomic oxygen chemistry.

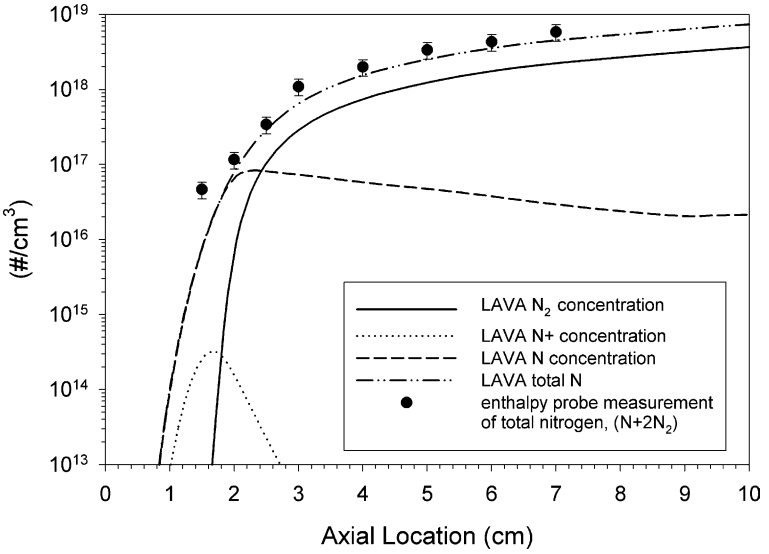


Fig. 9. Computational results for nitrogen chemistry compared to the measured total nitrogen.

even in the jet near field. The computed atomic oxygen ion ($O^+$) concentration, also shown in Fig. 8, never reaches significant levels for this flow field. Fig. 9 shows the calculated nitrogen species (N, $N^+$, $N_2$) and the computed total N ($N + 2N_2$) for comparison to the estimated total nitrogen from the enthalpy probe measurement [8], again along the jet centerline. The species $N^+$ and $N_2^+$ ($N_2^+$ is not shown in Fig. 9 because of its small magnitude) never achieve significant populations. The total amount of Ar ($Ar + Ar^+$) appears in Fig. 10 and is compared to enthalpy probe data [8]. Also shown in Fig. 10 is the calculated decay of the argon ion concentration and the equilibrium concentration corresponding to the calculated temperature. As the jet cools, the kinetics of recombination results in a relative overpopulation of argon ions.

Figs. 11–13 compare radial profiles of velocity, temperature, and entrained air fraction to enthalpy probe data, at various axial locations in the jet. In general the comparisons are acceptable, reproducing the general features of the flow field. Note that near the torch body the predicted velocity profile spreads more rapidly than

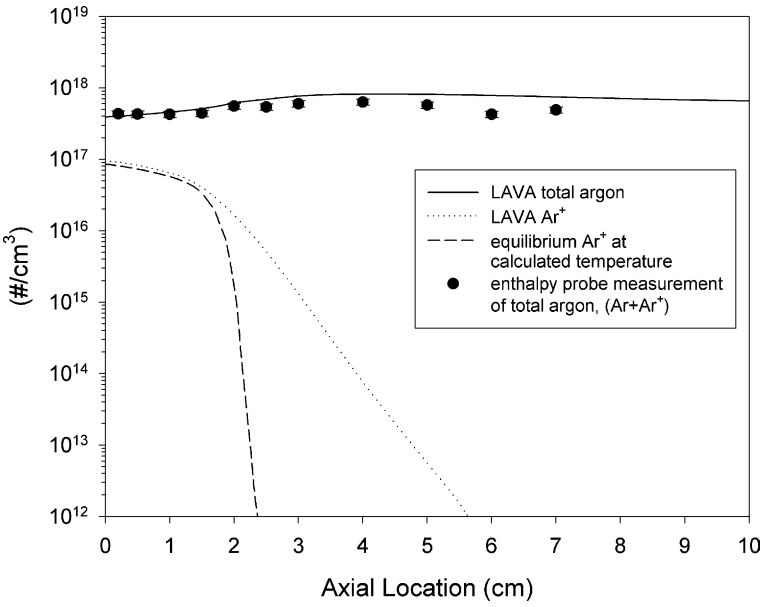


Fig. 10. Computational results for argon ionization–recombination compared to the measured total argon.

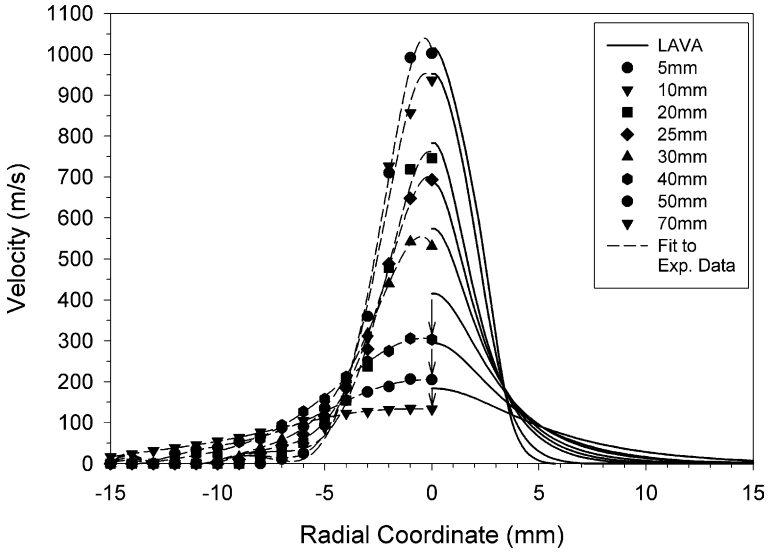


Fig. 11. Radial profile comparison of calculated results and enthalpy probe measurements of velocity. Distances in the legend are axial locations measured from the face of the torch.

the temperature profile with this trend reversing further downstream in the jet. This behavior is governed by the specific heat, which is rather non-linear due to strong temperature and composition dependencies. The relative spreading at a particular axial location (30 mm) is shown in Fig. 14, which compares the computed and measured temperature, velocity, and argon fraction (mass) radial profiles after normalization to the peak centerline value. LAVA predicts that the argon concentration should coincide closely with the temperature profile while the data suggests that argon fraction more closely coincides with the velocity profile even spreading at a slightly smaller rate than velocity in the jet periphery.

Radial profiles of the estimated molecular oxygen concentration obtained from the enthalpy probe and 2-photon LIF data [8] are compared to calculated results in Fig. 15. Again, the general features are represented, however, the logarithm ordinate, used because of the

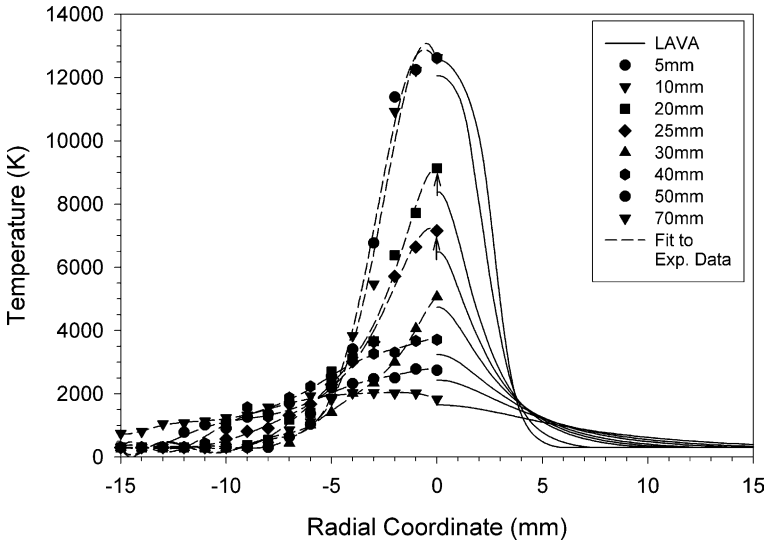


Fig. 12. Radial profile comparison of calculated results and enthalpy probe measurements of temperature. Distances in the legend are axial locations measured from the face of the torch.

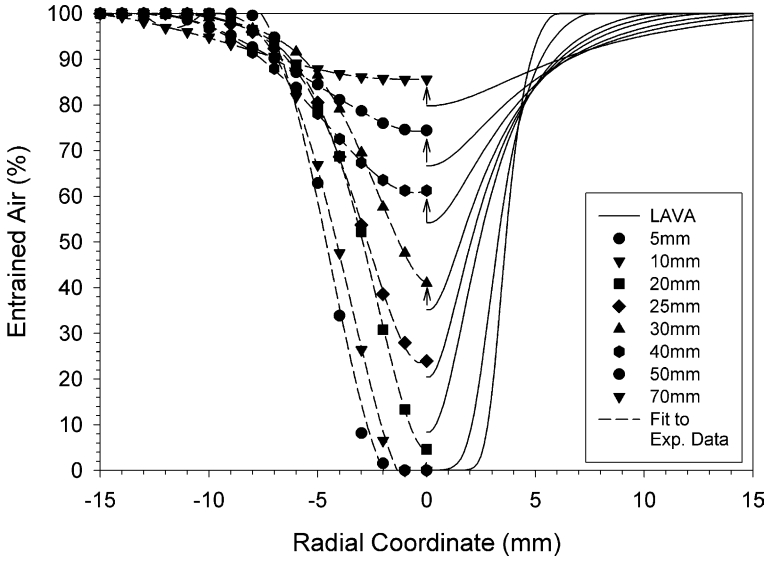


Fig. 13. Radial profile comparison of calculated results and enthalpy probe measurements of entrained air fraction. Distances in the legend are axial locations measured from the face of the torch.

large magnitude range, tends to compress differences. A more telling plot is the comparison between the measured and calculated atomic oxygen concentrations in Fig. 16. This data is presented on a linear scale. The model clearly over predicts the production of atomic oxygen in the shear layer as well as the diffusion of atomic oxygen into the periphery of the jet. Both are probably due to the incompleteness of mixing at the molecular scale. This result graphically illustrates the limitations of the $k$–$\varepsilon$ model in predicting chemistry with mixing.

## 5. Conclusions

The $k$–$\varepsilon$ representation of turbulent mixing used in the LAVA computational model is capable of reproducing, with fair accuracy, the general features of the

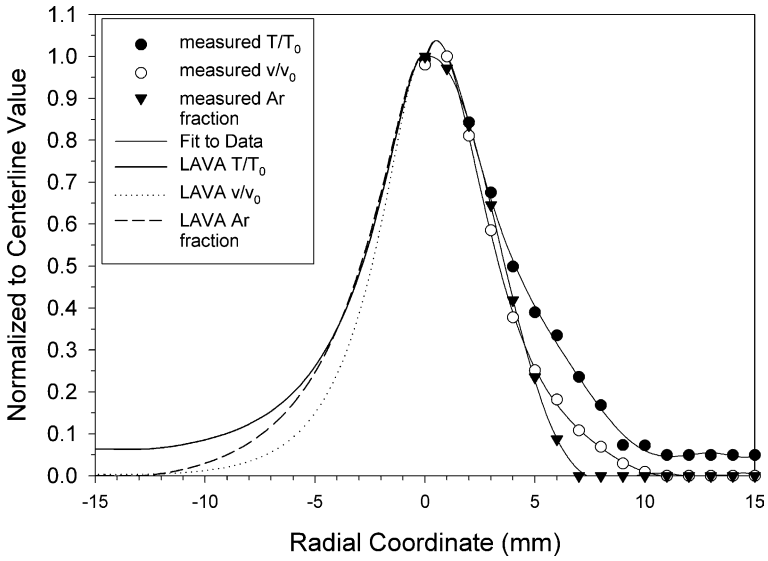


Fig. 14. Comparison of the calculated and measured radial spreading of the velocity, temperature and argon fraction, at an axial location of 30 mm.

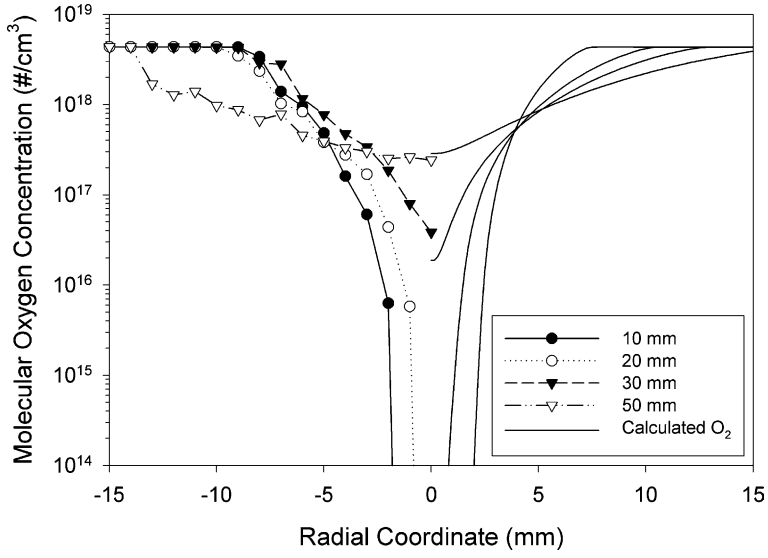


Fig. 15. Comparisons of calculated and measured (enthalpy probe) radial profiles of molecular oxygen concentration. Distances in the legend are axial locations measured from the face of the torch.

interaction of a plasma jet with its surrounding environment. The predictive capability is limited by the fact that inflow profiles must be specified. The results are dependent on both the magnitude and shape of the mean temperature and velocity profiles and on the shape and magnitude of the assumed turbulent kinetic energy profile. The results suggest that turbulent kinetic energy profiles that are characteristic of wall generated turbulence, i.e. do not approach zero until very near the wall, seem to produce better agreement with experiment. There is evidence to suggest that many thermal plasma jets have viscous, more or less laminar cores [40,41], and it is known that higher arc powers, resulting in higher velocities and higher temperature and viscosity, can result in relaminarization of an initially turbulent plasma jet [41].

The major limitation of the $k$–$\varepsilon$ turbulence model is in the shear layer where mixing and chemistry are pre-

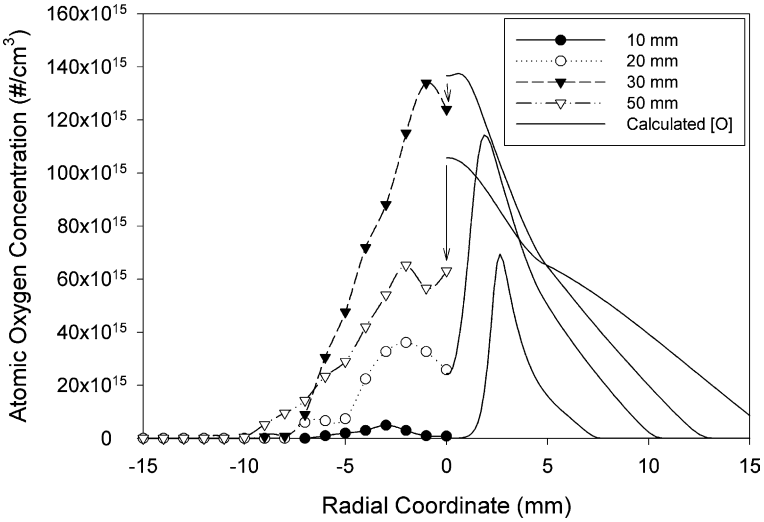


Fig. 16. Comparisons of calculated and measured (2 photon LIF) radial profiles of atomic oxygen concentration. Distances in the legend are axial locations measured from the face of the torch.

sent. While the $k$-model cannot accurately represent mixing with fast chemistry it can still provide useful prediction of plasma jet behavior, reproducing the major flow field characteristics. For the case of a plasma jet interacting with surround air, the dissociation chemistry is represented well enough to obtain reasonable agreement even though some details are distorted. For many applications, such as modeling particle heating and acceleration, this may be sufficient accuracy. For other applications, such as synthesis, or situations where radical species play a dominant role in homogeneous or heterogeneous chemical reaction, this may be an important limitation.

## Acknowledgements

This work was supported by the US Dept. Of Energy, Office of Energy Research, Office of Basic Energy Sciences, Division of Engineering and Geosciences, Engineering Research under DOE Idaho Field Office Contract DE-AC07-99ID13727.

## References

[1] E. Pfender, Y.C. Lee, Particle dynamics and particle heat and mass transfer in thermal plasma. Part I: The motion of a single particle without thermal effects, Plasma Chem. Plasma Process. 5 (1985) 211–237.

[2] X. Chen, E. Pfender, Effect of the Knudsen number on heat transfer to a particle immersed into a thermal plasma, Plasma Chem. Plasma Process. 3 (1983) 97–112.

[3] X. Chen, E. Pfender, Behavior of small particles in a thermal plasma flow, Plasma Chem. Plasma Process. 3 (1983) 351–366.

[4] Y.C. Lee, K.C. Hsu, E. Pfender, Heat transfer to particles in plasma flow, in: B. Waldie, G.A. Farnell (Eds.), Proceedings of the 5th International Symposium on Plasma Chemistry, Edinburgh, 1981, pp. 73–78.

[5] Y.P. Wan, V. Prasad, G.-X. Wang, S. Sampath, J.R. Fincke, Model and powder particle heating, melting, resolidification, and vaporization in plasma spraying processes, ASME J. Heat Transfer 121 (1999) 691–699.

[6] Y.P. Wan, J.R. Fincke, X.Y. Jiang, S. Sampath, V. Prasad, H. Herman, Modeling of oxidation of molybdenum particles during plasma spray deposition, Metall. Trans. 32B (2001) 475–481.

[7] Y.P. Wan, J.R. Fincke, S. Sampath, V. Prasad, H. Herman, Modeling and experimental observation of evaporation from molybdenum particles entrained in a thermal plasma jet, Int. J. Heat Mass Transfer 45 (2002) 1007–1015.

[8] J.R. Fincke, D.M. Crawford, S.C. Snyder, W.D. Swank, D.C. Haggard, R.L. Williamson, Entrainment in high velocity, high temperature thermal plasma jets. Part I: Experimental results, Companion paper to this work, 2003.

[9] K.D. Kang, S.H. Hong, Arc plasma jets of a nontransferred plasma torch, IEEE Trans. Plasma Sci. 24 (1996) 89–90.

[10] J.M. Bauchire, J.J. Gonzalez, A. Gleizes, Modeling of a DC plasma torch in laminar and turbulent flow, Plasma Chem. Plasma Process. 17 (1997) 409–432.

[11] B. Jodoin, P. Proulx, Y. Mercadier, Numerical study of supersonic direct current plasma nozzle flow, AIAA J. 36 (1998) 578–584.

[12] P. Han, X. Chen, Modeling of the subsonic–supersonic flow and heat transfer in a DC arc plasma torch, Plasma Chem. Plasma Process. 21 (2001) 249–264.

[13] J.D. Ramshaw, C.H. Chang, Computational fluid dynamics of multicomponent thermal plasmas, Plasma Chem. Plasma Process. 12 (1992) 299–325.

[14] C.H. Chang, J.D. Ramshaw, Numerical simulations of argon plasma jets flowing into cold air, Plasma Chem. Plasma Process. 13 (1993) 189–209.

[15] J.R. Fincke, C.H. Chang, W.D. Swank, D.C. Haggard, Entrainment and demixing in subsonic thermal plasma jets: comparison of measurements and predictions, Int. J. Heat Mass Transfer 37 (1994) 1673–1682.
[16] Ahmed, I.L. Bergman, Simulation of thermal plasma spraying of partially molten ceramics: effect of carrier gas on particle deposition and phase change phenomena, J. Heat Transfer 123 (2001) 188–196.
[17] B. Liu, T. Zhang, D.T. Gwane, Computational analysis of the influence of process parameters on the flow field of a plasma jet, Surf. Coat. Technol. 132 (2000) 202–216.
[18] H. Li, X. Chen, Three-dimensional simulation of the turbulent plasma jet impinging upon a flat plate and with transverse particle and carrier gas injection, Plasma Chem. Plasma Process. 22 (2002) 27–57.
[19] G. Mariaux, P. Fauchais, A. Vardelle, B. Pateyron, Modeling of the plasma spray process: from powder injection to coating formation, High Temp. Mater. Process. 5 (2001) 61–85.
[20] P.C. Huang, H. Heberlein, E. Pfender, A two fluid model of turbulence for a thermal plasma jet, Plasma Chem. Plasma Process. 15 (1995) 25–37.
[21] R. Ye, P. Proulx, M.I. Boulos, Turbulence phenomena in the radio frequency induction plasma torch, Int. J. Heat Mass Transfer 42 (1999) 1585–1595.
[22] Y.C. Lee, E. Pfender, Particle dynamics and particle heat and mass transfer in thermal plasmas. Part III: Thermal plasma jet reactors and multiparticle injection, Plasma Chem. Plasma Process. 7 (1987) 1–27.
[23] F.A. Williams, Combustion Theory, Benjamin/Cummings, Menlo Park, California, 1985 (p. 393).
[24] J.K. Dukowicz, A particle-fluid numerical model for liquid sprays, J. Comput. Phys. 35 (1980) 229–253.
[25] P.J. O'Rourke, Statistical properties and numerical implementation of a model for droplet dispersion in a turbulent gas, J. Comput. Phys. 83 (1989) 345–360.
[26] A.A. Amsden, J.D. Ramshaw, P.J. O'Rourke, J.K. Dukowicz, KIVA: A computer program for two- and three-dimensional fluid flows with chemical reactions and fuel sprays, LA-10245-MS, Los Alamos National Laboratory Report, 1985.
[27] J.D. Ramshaw, Self-consistent effective binary diffusion in multicomponent gas mixtures, J. Non-Equilib. Thermodyn. 15 (1990) 295–300.
[28] M. Desilets, P. Proulx, G. Soucy, Modeling of multicomponent diffusion in high temperature flows, Int. J. Heat Mass Transfer 40 (1997) 4273–4278.
[29] C.H. Chang, J.D. Ramshaw, Numerical simulation of nonequilibrium effects in an argon plasma jet, Phys. Plasma. 1 (1994) 3698–3708.
[30] J.H. Park, E. Pfender, C.H. Chang, Reduction of chemical reactions in nitrogen and nitrogen–hydrogen plasma jets flowing into atmospheric air, Plasma Chem. Plasma Process. 20 (2000) 165–181.
[31] J.R. Fincke, W.D. Swank, D.C. Haggard, Plasma spraying of alumina: plasma and particle flow fields, Plasma Chem. Plasma Process. 13 (1993) 579–600.
[32] M.I. Hoffert, H. Lien, Quasi-one-dimensional, nonequilibrium gas dynamics of partially ionized two-temperature argon, Phys. Fluids 10 (1967) 1769–1777.
[33] T.G. Owano, C.H. Kruger, Electron–ion three-body recombination coefficient of argon, AIAA J. 31 (1993) 75–82.
[34] M.I. Hoffert, Precursor ionization effects on magneto-hydrodynamic switch-on shock structure, J. Plasma Phys. 4 (1970) 477–494.
[35] M. Mitchner, C.H. Kruger Jr., Partially Ionized Gases, Eilet-Interscience, New York, 1973.
[36] C. Olikara, G.L. Borman, A computer program for calculating properties of equilibrium combustion products with some applications to I.C. engines, SAE Paper 750468, 1975.
[37] J.H. Park, Nonequilibrium Hypersonic Aerodynamics, Wiley, New York, 1990.
[38] M.W. Chase Jr., C.A. Davies, J.R. Downy Jr., D.J. Frurip, R.A. McDonald, A.N. Syverud, JANEF Thermochemical Tables Third Edition, J. Phys. Chem. Ref. Data 14 (Suppl. 1) (1985).
[39] H.W. Drawin, P. Felenbok, Data for Plasmas in Local Thermodynamic Equilibrium, Gauthier-Villars, Paris, 1965.
[40] M.A. Leschziner, W. Rodi, Computation of strongly axisymmetric free jets, AIAA J. 22 (1984) 1742–1747.
[41] E. Pfender, J.R. Fincke, R. Spores, Entrainment of cold gas into thermal plasma jets, Plasma Chem. Plasma Process. 11 (1991) 529–543.
[42] J.R. Fincke, G.C. Pentecost, Laminar to turbulent transition and entrainment in thermal plasma jets, in: Proceedings of the 28th National Heat Transfer Conference Heat Transfer in Thermal Plasma Processing, HTD-vol. 161, American Society of Mechanical Engineers, 1991, pp. 101–106.
[43] J.O. Hinze, Turbulence, McGraw-Hill, New York, 1975 (p. 639, 641, 725).